An experiment generates a specified mean strained rate turbulent flow: Dynamics of particles

Special Collection: Turbulence in Plasmas and Fluids

R. Hassanian ✉ 🅘 ; Á. Helgadóttir 🅘 ; L. Bouhlali; M. Riedel 🅘

Check for updates

View Online

Export Citation

Articles You May Be Interested In

Deciphering the dynamics of distorted turbulent flows: Lagrangian particle tracking and chaos prediction through transformer-based deep learning models

Physics of Fluids (July 2023)

Large-eddy simulation of low frequency oscillations of the Dean vortices in turbulent pipe bend flows

Physics of Fluids (February 2005)

Drag modulation by inertial particles in a drag-reduced turbulent channel flow with spanwise wall oscillation

Physics of Fluids (October 2024)

An experiment generates a specified mean strained rate turbulent flow: Dynamics of particles

View Online   Export Citation   CrossMark

R. Hassanian,[1,a] Á. Helgadóttir,[1] L. Bouhlali,[2] and M. Riedel[1,3]

AFFILIATIONS

[1]The Faculty of Industrial Engineering, Mechanical Engineering, and Computer Science, University of Iceland, 102 Reykjavík, Iceland
[2]Reykjavik University, 102 Reykjavik, Iceland
[3]Juelich Supercomputing Centre, 52428 Jülich, Germany

Note: This paper is part of the special topic, Turbulence in Plasmas and Fluids.
[a]Author to whom correspondence should be addressed: seh@hi.is

ABSTRACT

This study aimed to simulate straining turbulent flow empirically, having direct similarities with vast naturally occurring flows and engineering applications. The flow was generated in $100 < Re_\lambda < 500$ and seeded with passive and inertial particles. Lagrangian particle tracking and particle image velocimetry were employed to extract the dynamics of particle statistics and flow features, respectively. The studies for axisymmetric straining turbulent flow reported that the strain rate, flow geometry, and gravity affect particle statistics. To practically investigate mentioned effects in the literature, we present the behavior of both passive and inertial particles from the novel experiment conducted on initially homogeneous turbulence undergoing a sudden axisymmetric expansion. We represent the result with two different mean strains and Reynolds–Taylor microscales. However, this study, in contrast to the previous studies, considers the fields of inertial particles in the presence of gravity. The result discloses that the novel designed and conducted experiments simulated the flow satisfactorily. Then, the particle behavior in such flow showed the effectiveness of the flow distortion on particle dynamics such as velocity root mean square and Reynolds stress. Straining turbulence flow is subject to many industrial applications and physics studies, such as stagnation points, external flow around an airfoil, internal flow in changeable cross section pipe, expansion in the engine mixing chamber, and leading edge erosion. This study's conclusion could apply constructively to these areas.

I. INTRODUCTION

The dynamics of particles in turbulent flow relate to a broad range of natural phenomena and engineering applications.[1] The distribution of pollutants in the atmosphere, the formation of rain in a cloud,[2] and the spread of sediments in oceans and rivers are instances.[3] Many industrial applications are related, including internal engine combustion, particle interaction in a mixing chamber,[4] and leading-edge[5] erosion in compressors and turbines.[6,7] The external flow over the airfoil[8,9] and internal flow in changeable cross-section pipe[10–12] are instances of straining turbulence flow.[13,14] This study's motivation has been from recent works that examined the Lagrangian inertial particle in shear flow[12–14] and boundary layer,[15,16] reporting a profound effect on inertial particle statistics. Later, Lee *et al.*[17] showed that the mean strain rate substantially affected tracer and inertial particle statistics. They reported that for a higher strain rate, acceleration variance increased notably.[17] They also noticed that large-scale motion could

affect particle motion, and the heavier inertial particles represent lower acceleration variance than the lighter inertial particles.[17]

Most natural flows combine inertial particles and straining geometries;[18,19] thus, the straining motion consideration is essential. It is well addressed that turbulent flow statistics[1,20] are applicable.[21–23] Due to inertia and interaction, the lighter inertial particle to mean flow has higher acceleration than the tracer particle.[17] When the particle has higher inertia, the ballistic motion will increase the mean flow acceleration.[17] The straining motion appears in the stagnation point region.[17] It has been known that extra fluctuation is derived from mean strain and transmitted to the turbulence.[20,21] Most studies focused on Lagrangian acceleration particle statistics in isotropic turbulence flow, but the recent literature mentioned the vitality of large anisotropic scale Lagrangian dynamics.[17] The small scale may be isotropic, but the large scale is highly anisotropic.[24] Indeed, flow with mean zero flow is generally isotropic, not realistic, and usually close to being

anisotropic.[20] The large-scale structure depends on initial turbulence conditions.[20] Local strain rates in mean flow do not control it although the magnitude of Reynolds stress is related to the immediate history of turbulence which can say the scales have a remote feeling.[20] Statistics of the scales are not a function of local gradients in the mean flow.[20] Moreover, its specified gravity and strain affect the acceleration variance and Stokes number, narrowing the acceleration probability distribution function (p.d.f.s) and skewed with inertia.[17]

The current work designs and suggests a novel procedure to simulate a turbulence flow with a specified strain rate in the laboratory environment. Tracer particles seeded the flow, and the particle image velocimetry (PIV) technique was employed to extract the flow feature. Furthermore, to examine the dynamics of the particles affected by turbulence intensity, mean strain rate, and presence of gravity,[25,26] inertial and tracer particles were seeded the flow in separate implementations, and the Lagrangian particle tracking (LPT) approach was applied to investigate the particle behaviors. The proposed procedure applies to many industrial applications, particularly stagnation point and flow with various geometry. Furthermore, it manifests sight to study the particles in the natural environment and variant flow conditions.

This study presents velocity root mean square (RMS) and normalized Reynolds stress results. In addition to the novel procedure, the examination is conducted in the presence of gravity,[26,27] not considered in the previous numerical studies that have examined the inertial particles' dynamics in the turbulent flow.[23,28] It is well determined that the conclusions achieved in zero gravity should not be applied outside this condition.[27,29] Therefore, it is essential to understand the gravity effects on the dynamics of the particles. Hence, this paper is organized as follows: the applied theory for the dynamics of the particles is presented in Sec. II. The experiment is explained in Sec. III, and the measurement method is explored in Sec. IV. Results and discussion are represented in Sec. V and Sec. VI provides the conclusions.

II. THEORY

In this section, the applied theory in turbulent flow statistics is described. Since the data are extracted from measurement, it is essential to define the characteristics of the flow and particle properties and how the measured data are used to investigate the dynamics of a particle and flow feature.

A. Strained turbulence

The turbulent flow is generated with the action of impeller rotors in the corners of a box turbulence facility. The turbulent flow is then strained in the vertical direction (see Fig. 1) by the motion of flat circular plates, as shown in the sketch. The fluid is seeded with buoyant (tracer) particles and inertial particles with median diameters 8–10 μm and 210–250 μm, respectively. The specific gravity for tracers was 1.1 g/cm³ (hollow glass) and 2.5 g/cm³ (solid glass) for inertial particles. The flow field properties are obtained through the particle image velocimetry (PIV), and the Lagrangian particle tracking (LPT) method is employed to study the particles' movement. Equation (1) describes the mean flow field in the facility

$$\langle \mathbf{U} \rangle = (Sx, -2Sy, Sz), \tag{1}$$

where $-2S$ is the primary strain rate in the Y-dir; S is the strain rate for the other two directions; and x, y, and z are the particle location. In
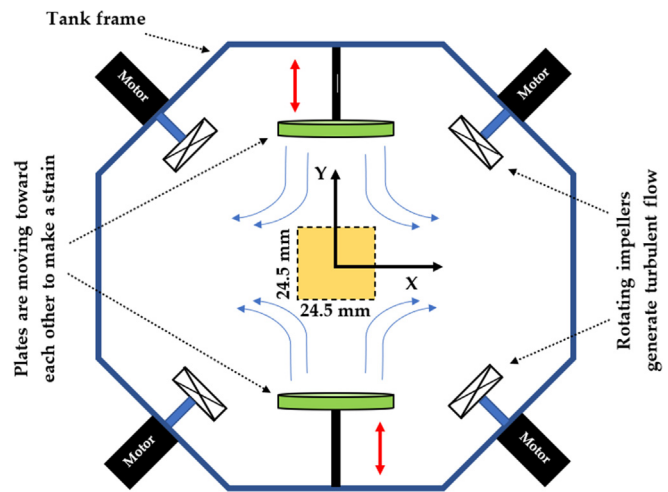

FIG. 1. A sketch of the tank facility and the location of the LPT/PIV measurement area. The viewing window (24.5 × 24.5 mm²) is located in the center of the water tank. The Y-axis of the coordinate system (CS) points upwards, whereas the X-axis points from left to right. The origin of the CS is located at the center point of the tank.

this work, the flow is considered in two-dimensional (2D); therefore, Z-dir is not addressed.

The straining flow cases in the experiment were created with two mean strain rates, $2S = 4 \, \text{s}^{-1}$ and $2S = 8 \, \text{s}^{-1}$. Equation (1) is based on the laminar flow; however, we know that velocity fluctuates in the turbulence flow. Further details on the experimental setup are described in Sec. III. Based on the determined coordinate system (CS) in this experiment, the strain rate for both directions has these notations:[1] $dU_y/dy = -2S$ and $dU_x/dx = S$.

B. Turbulent flow characterization

The turbulence flow statistics were used to extract the flow field properties. We analyzed the trajectories of particles in the flow field using the LPT technique. Accordingly, the velocity fluctuations u_x and u_y can be calculated as

$$u_i = U_i - \langle U_i \rangle, \quad i = x, y, \tag{2}$$

where U is the measured (total) velocity, $\langle U \rangle$ is the mean velocity, and the subscript i refers to the component of the velocity, in x, y (or z) direction.

We applied the following equations to obtain the variance of velocity $var(U_i)$, and the velocities RMS $u_{rms,i}$:

$$u_{rms,i} = \sqrt{var(U_i)} = \langle u_i^2 \rangle^{1/2}. \tag{3}$$

Reynolds-stress is a term that stems from momentum transfer by fluctuating velocity field.[1] Reynolds-stresses are the components of a second-order tensor, which is symmetric. The diagonal components $\langle u_i u_i \rangle$ are normal stress, while the off diagonal components $\langle u_i u_j \rangle$ are shear stress (the subscripts i and j denote the components of the velocity).[1] It has been addressed the Reynolds stress gaining from the irrotational field has definitely no effect on the mean velocity field.[1] The normalized Reynolds-stress is calculated for particles in this work to

examine the fluctuation of particles caused by distinct strain rates and turbulence intensity. The definition for the normalized Reynolds-stress is[1]

$$(u_i^2)/2k_0 = (u_i^2)/(u_{0,x}^2 + u_{0,y}^2), \quad i = x, y, \tag{4}$$

where u is the particle velocity in the deformed flow; $u_{0,x}$, $u_{0,y}$ are the velocity; $k_0 = (u_{0,x}^2 + u_{0,y}^2)/2$ is the turbulent kinematic energy of the particle in turbulent flow without strain; and the subscript i denotes the components of the velocity. Since the measurement is carried on in 2D in this work, the velocity has two components in the x and y directions.

The number of points used to compute statistics depends on the type of experiment conducted. The turbulence energy dissipation rate is calculated using a second-order longitudinal velocity structure function $D_{LL}(r)$, assuming inertial subrange $D_{LL}(r) = C_2(\varepsilon r)^{1/2}$ with a universal constant $C_2 = 2.1$,[1] r is the separation and $U_i(x, t)$ is Eulerian velocity field.

$$\begin{aligned} D_{LL}(r) &= D_{ij}(r, x, t) \\ &= \langle [U_i(x+r, t) - U_i(x, t)][U_j(x+r, t) - U_j(x, t)] \rangle. \end{aligned} \tag{5}$$

The mean energy dissipation rate is constant in the inertial subrange, as illustrated in the results. We used the Eulerian autocorrelation function $\rho(L)$ to obtain the Eulerian integral scale l, which can be defined as:[1,30]

$$\rho(L) = \langle u(r_0 + L)u(r_0) \rangle / u^2. \tag{6}$$

The Eulerian integral scale is given by[1,30]

$$l = \int_0^\infty \rho(L) dL. \tag{7}$$

In Eq. (7), the velocity is taken on a grid obtained from the particle image velocimetry (PIV) measurements, and r_0 is taken in both the x and y directions; L is the Eulerian integral variable. Based on Kolmogorov's hypothesis, the length and time scales of the turbulence flow can be calculated using the following equations:

$$\eta = (\nu^3/\varepsilon)^{1/4}, \tag{8}$$
$$\tau_\eta = (\nu/\varepsilon)^{1/2}, \tag{9}$$

where ν is the kinematic viscosity of the fluid, η is Kolmogorov's length scale, τ_η is the Kolmogorov's timescale, and ε is the energy dissipation rate which is evaluated via described second-order longitudinal velocity structure function.

C. Stokes number

In this study, we employed LPT to track the particle in the generated flow. Therefore, the Stokes number must be considered for both particle types. The Stokes number specifies whether a particle introduced to the flow will follow the flow streamline or not. This identification is defined by the following equation:

$$S_t = \tau_p/\tau_\eta, \tag{10}$$

where τ_p is Stokes' relaxation time. Kolmogorov scale is based on the flow quantities before applying the strain, and these amounts are

calculated for two-particle types and presented in Sec. IV. Stokes' relaxation time τ_p is, in turn, calculated by the following equation:

$$\tau_p = \rho_p d_p^2/18\mu, \tag{11}$$

where ρ_p is the particle density, d_p is a spherical particle diameter, and μ is the dynamic fluid viscosity that, in this experiment, is water. Both the Stokes' relaxation time and the Kolmogorov timescale are required in Eq. (9). The relaxation time for each particle is calculated based on the particle property from Eq. (10). The Stokes number significantly greater than 1 ($St \gg 1$) describes particles that are unaffected by a fluid velocity change and continue their original trajectory; if ($St \ll 1$), the particle will follow the fluid's local velocity.

III. EXPERIMENT

The flow facility at the Laboratory for Fundamental Turbulence Research (LFTR) at Reykjavik University is shown in Fig. 2, where the experiments were carried out in a zero-mean turbulence box (with the corners cut off to facilitate impellers that force the flow). The tank is specifically designed for studying turbulence (Lagrangian and Eulerian motion at moderate Reynolds numbers). This flow facility produces a nearly stationary homogeneous isotropic turbulence near the center of the tank, where measurements are performed. The water tank ($60 \times 60 \times 60$ cm^3) has 20 mm thick acrylic walls (transparent Plexiglas XT) that enable optical access to the data. The eight corners of the box have a triangular shape, while the top and the bottom are nearly circular. An aluminum frame holds the components of the turbulence box together. The turbulence is generated by eight impellers driven by independently controlled servo motors (Lenz-model: MCS), which are mounted at the cube's eight corners and point to the center of the tank. The rotation rate of each servo motor is adjustable over a range of 100–4500 revolutions per minute (rpm) at a gearing rate of 0.075. The motion-view filtering software that came with these motors was used to monitor and set up the suited speed of each impeller. The degassing system was used to remove bubbles and solid dust from the water before starting the experiment.
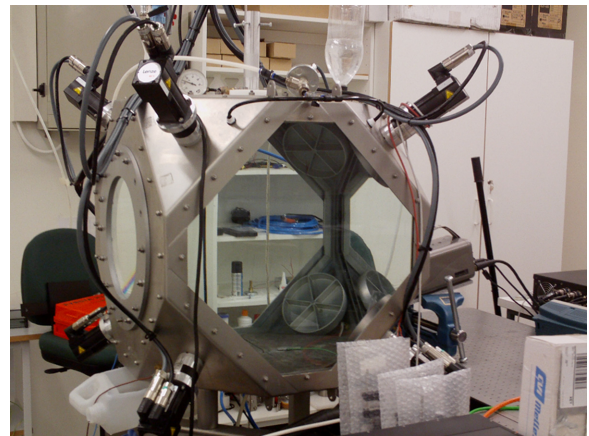

FIG. 2. A photo of the turbulence box taken at the Laboratory for Fundamental Turbulence Research (LFTR) at Reykjavik University.[31,32] Reproduced with permission from Hassanian, M.S. dissertation (Reykjavik University, 2020). Copyright 2020 Author.

Circular plates, shown at the top and bottom (see Fig. 1), generate the strain motions; a linear actuator drove each plate with a piston rod (Parker, model: ETV32M10PA47JMA400A). When they are moved toward the center with a pre-described rate that ensures a nearly constant strain rate in the fluid. For each flow case, variables are investigated with different propeller rotation rates, strain rates, and particle types; a total of 20 piston movements is recorded to collect a sufficient number of particle trajectories. Each video is statistically independent, as the flow is given ample time to recover to near isotropy between different strokes. The recording area is 24.5×24.5 mm^2 and is located in the center of the tank for LPT/PIV measurements (Fig. 1). The flow case in this study depends on the size of the particles and the rotation speed of the impeller in the tank and is applied at 1000 and 1500 rpm. Two circular plates described previously created two mean strain rates: $2S = 4$ and $2S = 8$ s^{-1}. The plate driver motor moves according to an exponential profile, and the same as a particle would move by if it were moving along the y-axis toward the center of the coordinate system. The straining turbulence flow was generated for two kinds of particles: a passive and an inertial particle. Each particle has two nominal strain rates and two impeller rotation speeds as the numerical variations of the turbulence factor. The detection system for LPT was set at 10 kHz [10 000 frames per second (fps)] for well-resolved particle velocity and acceleration statistics. This very high temporal resolution (0.1–0.2 ms) is considerably smaller than the Kolmogorov time τ_η (35–99 ms) of the smallest eddies present in the flow, which is determined in Sec. V; therefore, the properties of the energy dissipation rate range in the flow are solved. For each flow case, the average of the measurements was done over 20 videos in the same instant time, and one averaged data file was created. The average file was used to obtain the flow field properties. The software includes several stages. First, it converts the image to a readable file, processes it to achieve the necessary data, and follows the post-processing stages.

IV. MEASUREMENT TECHNIQUE
A. Particle image velocimetry technique

The particle image velocimetry (PIV) technique is applied and extracts the flow properties before strain deformation. Thus, via a second-order longitudinal velocimetry structure function, the turbulent flow dissipation rate is obtained; therefore, the Kolmogorov time-scale is calculated based on Eq. (9) and Stokes number obtained from Eq. (10). In this study, the PIV has been applied independently of the LPT experiment because the number of seeded particles in PIV is much higher. The PIV measurement is applied to extract the flow characteristics. A single high-speed CMOS camera with a 105 mm focal length lens was used to record the PIV images, and it was set at 512×512 pixels resolution. For the illumination of the tracer particles, an Nd-YAF laser (527 nm) was used and synchronized at the same sampling frequency as the camera. The laser was set at internal mode, 14 A Q-switch current, and pulse width of 2.5 μs. The laser beam is expanded to a sheet along the (X, Y)-plane using spherical and cylindrical lenses. The sample area has a size of the frame and thickness equal to the thickness of the laser sheet, which is 2 mm. The PIV configuration 2C-2D is applied (see Fig. 3), which delivers two velocity components in the x and the y directions.[33] In this configuration, one
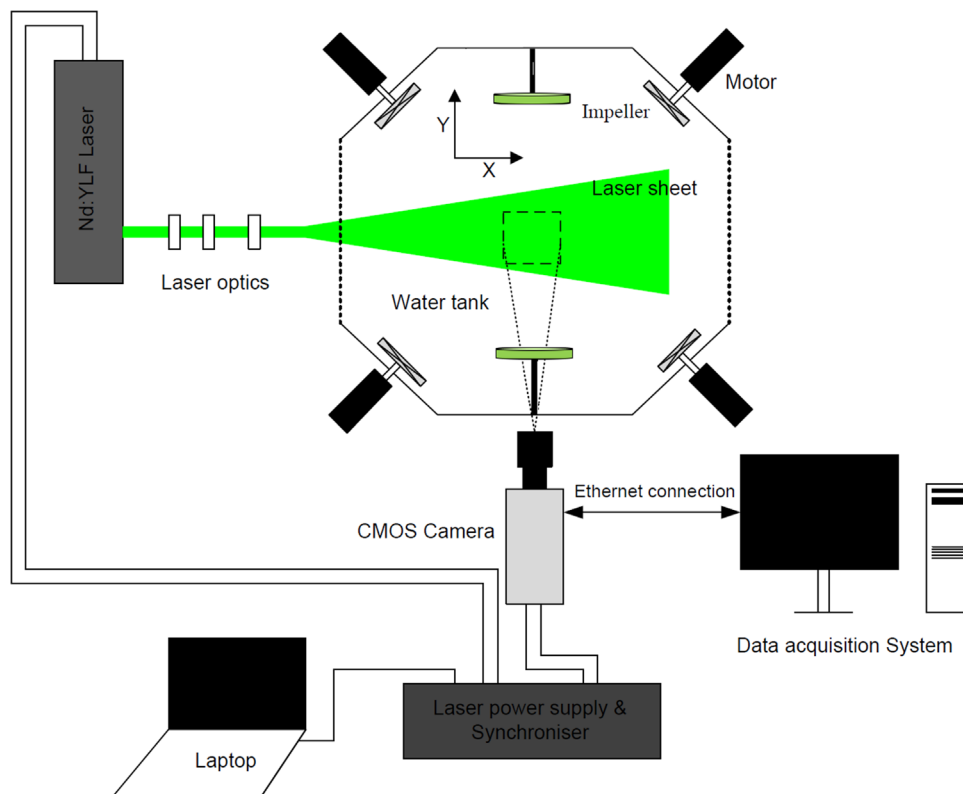

FIG. 3. A view of the experiment set up to record the PIV/LPT frames.

20 January 2025 14:54:21

camera is used, and its position is perpendicular to the laser light sheet. The displacement of the particles is estimated using cross correlation and fast-Fourier transformers. For evaluation of recorded images, the digital PIV recording is divided into small subareas called interrogation areas (IA).[33] It is assumed that all particles within one IA have moved homogeneously between two illuminations. In order to obtain a valid velocity measurement, a spot should contain anywhere from seven to ten particle pairs, where one pair refers to a particle imaged at both t and t'.[33] In the literature, it is noted it is advantageous to offset the second IA according to the mean displacement of the tracer particles between the two illuminations,[34] which is performed. Regarding the particle seeding in the flow, ideally, the particle should have the same density as the flow, which is respected in this study by the tracer particle. Another important factor in the measurements' accuracy is the seeding's homogeneity. The applied PIV recording technique is based on the method which provides a single illuminated image for each illumination pulse (multi-frame/single exposure PIV) since the used CMOS camera and laser are internally synchronized at the same frequency rate. In the current study, the PIV recording system is able to employ the double-frame/single-exposure recording technique. The measurement area of size 512×512 pixels ($24.5 \times 24.5\,\mathrm{mm}^2$) was divided into interrogation areas (IA) of size 64×64 pixels. To compute the structure functions from PIV, the IA has a size of 64×64 pixels with an overlap of 50% to decrease the computing time. This yielded 15×15 velocity vectors with a spacing grid of 32 pixels. The local displacement vector for the images of the tracer particles of the

first and second illumination is determined for each IA utilizing statistical methods (cross correlation). The projection of the vector of the local flow velocity into the plane of the light sheet (two-component velocity vector) is calculated respecting the time delay between the two illuminations and the magnification at imaging. The interrogation process is repeated for all IA's of the PIV recording and was delivered a complete velocity field. The PIV was conducted with similar turbulence intensity to LPT data and has controlled by a servomotor at speeds of 1000 and 1500 rpm without an act of strain. The frame rate set up was 2 kHz [2000 frames per second (fps)], which gives an exposure time (time interval between two successive frames) of 500 μs (0.5 ms). The recorded videos were 20 for each experiment, where each video has 1000 frames; this gives 20 000 instantaneously recorded images. This work applies a fast-Fourier transformer, a strong tool to accelerate the correlation process in digital PIV. The measurement represents the the Taylor microscale Reynolds number[1,21] range is 100–500 in the performed experiment.

B. Lagrangian particle tracking measurements

The Lagrangian particle tracking (LPT) measurements were carried out for two flow cases in this work in the presence of the strain. The camera and laser setup for LPT measurement are as explained in the PIV measurement. LPT uses a lower seeding density but finds individual and longer particle tracks. One camera was used in the LPT system, enabling the reconstruction of particle tracks in two dimensions.
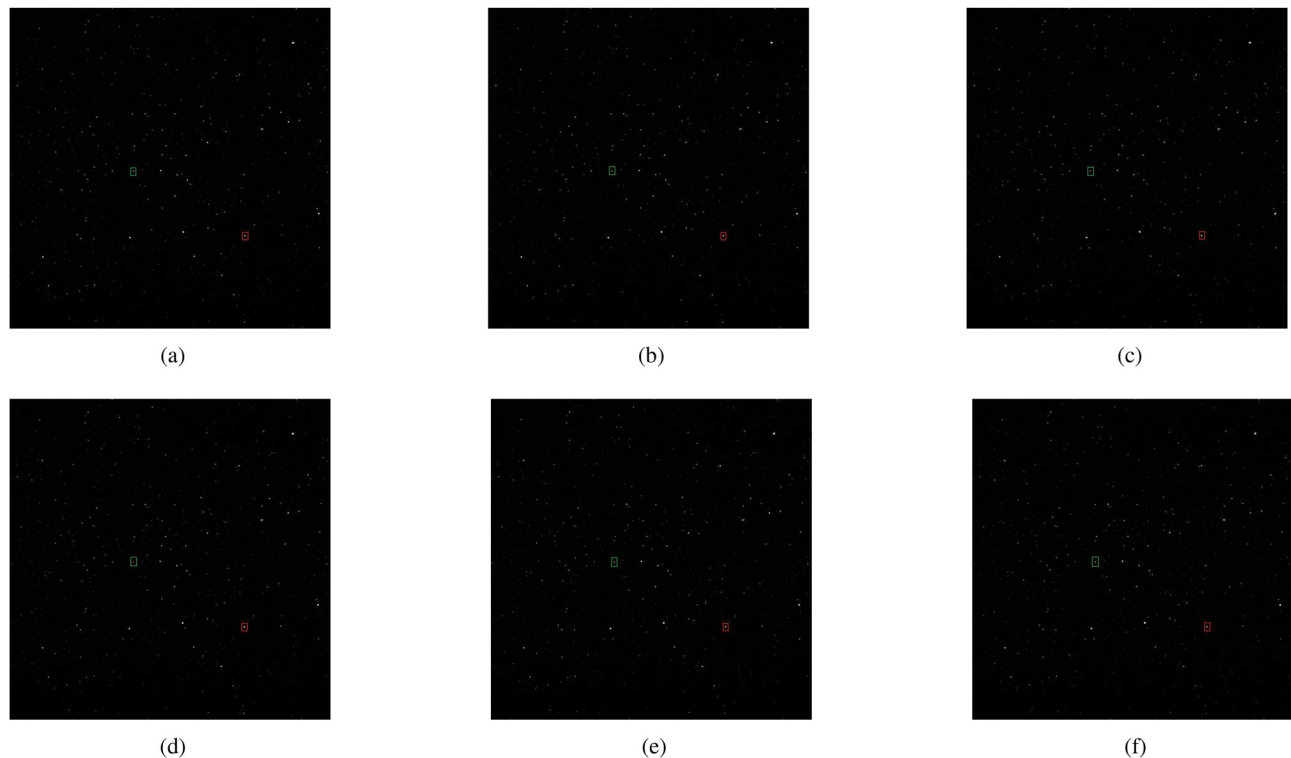

| (a) | (b) | (c) |
| (d) | (e) | (f) |

FIG. 4. A representation of six sequential frames of the recording via a high-speed camera in the LPT technique: (a) frame 1 at $t\,s$, (b) frame 2 at $t + 0.0001$ s, (c) frame 3 at $t + 0.0002$ s, (d) frame 4 at $t + 0.0003$ s, (e) frame 5 at $t + 0.0004$ s, and (f) frame 6 at $t + 0.0005$ s (t is an arbitrary moment). Each frame has been taken in 0.0001 s. The green and red boxes display the locations of two different particles in each time frame.

These particle tracks are used to calculate the dynamics of particles of initial turbulence, including the Lagrangian statistics. Figure 4 illustrates LPT frames recorded and how particles are seen and could be tracked. The particles' center detection (identification) method used in this LPT technique is called the 2D Gaussian fitting; its principle is based on the idea that a Gaussian can approximate particles' intensity profile, and therefore, the Gaussian function can be used to fit this intensity profile of the particle image. For each particle pixel group, two one-dimensional Gaussian fits[35] are used: one Gaussian will determine the horizontal position of the particle, and the second will determine the vertical position and, hence, solving the two system of equations:

$$I_i = \frac{I_0}{\sqrt{2\pi}\sigma}\exp\left[-\frac{1}{2}\left(\frac{x_i - x_c}{\sigma}\right)^2\right], \quad (12)$$

$$I_i = \frac{I_0}{\sqrt{2\pi}\sigma}\exp\left[-\frac{1}{2}\left(\frac{y_i - y_c}{\sigma}\right)^2\right], \quad (13)$$

for $i = 1, 2, 3$, it leads to particle center coordinates (x_c, y_c). Notation (x_i, y_i) are the coordinates of the local maximum pixel intensity I_2 and the two neighbor's pixel intensities I_1 and I_3, σ is the width of the distribution that is assumed equally in x and y coordinates, and I is the pixel intensity. Notice that the captured images are dynamically thresholded before starting the process of detecting the particles. It is assumed that every local maximum in intensity above a threshold represents a particle. Once particle centers on each image are detected, the next step is reconstructing their 2D tracks from successive images by matching each particle's position in the first image with its corresponding position in the second image.

The four-frame particle tracking technique used in this work, which is called four-frame Best Estimate,[36] is an extension of the four-frame Minimum Change in Acceleration heuristic (4MA);[36] it tracks a particle path through four sequential flow images (see Fig. 5) by a prediction which is based on a given heuristic and cost function. This method proceeds in two steps. First, the center of a search region is calculated using a constraint on velocity or acceleration.

Then, all particles within the search region are tested using a cost function that has to be minimized. Let x_i^n denotes the ith position in the nth frame. A tracking algorithm, then, tries to find an x_j^{n+1} for each x_i^n such that x_j is the position of the particle in the frame $[n + 1]$ that was at position x_i in the frame $[n]$. The most common is restricting the number of frames over which the cost-tracking function is optimized. The second approximation is to restrict the x_j^{n+1} investigated as possible matches for each x_i^n by imposing a limit on the distance a particle can travel from one frame to the next. Within these approximations, a tracking algorithm is specified by two parameters: the heuristic used to calculate the cost function and the method used to break tracking conflicts. In this process, if more than one track shares the same particle, the incorrect tracks are discarded. The position of the particle in the frame $[n + 1]$ is estimated by using the three-frame Minimum Acceleration heuristic (3MA)[36] which is given by

$$x_i^{n+1} = x_i^n + U_i^n \Delta t = 2x_i^n - x_i^{n-1}, \quad (14)$$

where U_i^n is the estimated velocity and Δt is the time elapsed between frames. For each of the particles in the search volume search region: S1 in the frame $[n + 1]$, a position x_i^{n+2} in the frame $[n + 2]$ is estimated to be[36]

$$x_i^{n+2} = x_i^n + U_i^n 2\Delta t + a_i^n \Delta t^2, \quad (15)$$

where a_i^n is the estimated particle acceleration. Particles in a search region: S2 around it are investigated. The particle chosen as the best match in the frame $[n + 2]$ is the one that has the smallest distance between particles in the frame $[n + 2]$ and the second estimated position, and hence, the particle that is linked here in the previous frame $[n + 1]$ is chosen as the best match too. The cost function ϕ_{ij}^n applied in this case is given by[36]

$$\phi_{ij}^n = ||x_j^{n+2} - x_i^{n+2}||, \quad (16)$$

where x_i^{n+2} is the estimated position in the frame $[n + 2]$. The simplest way to handle conflicts is to give up: when a particle in the frame $[n + 1]$ is the best match for multiple particles in the frame [n], the
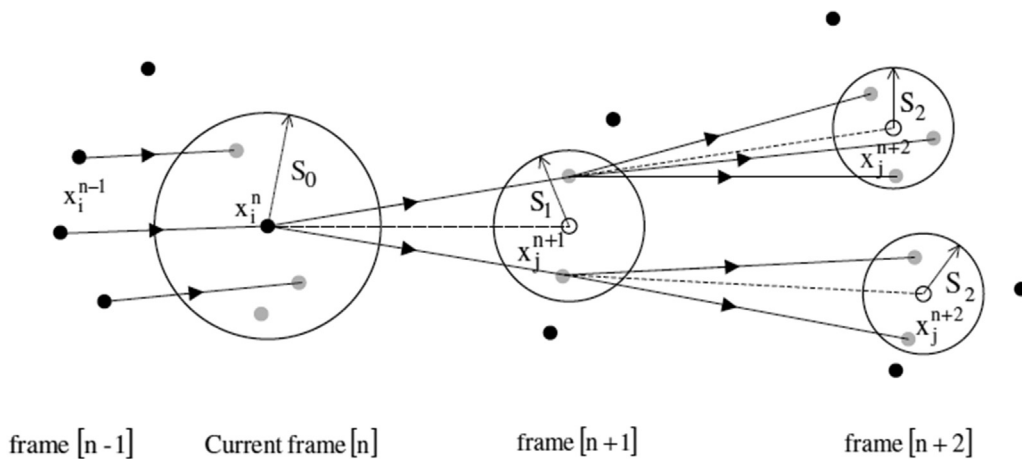

FIG. 5. Schematic diagram of the conventional four-frame PTV tracking algorithm. The black circles are the particles positioned outside of the search region, while the light gray circles are the particles positioned inside the search region, and the white circles are the predicted positions of the particles in the next frame. The arrows that link the frames between them are the possible particle path.
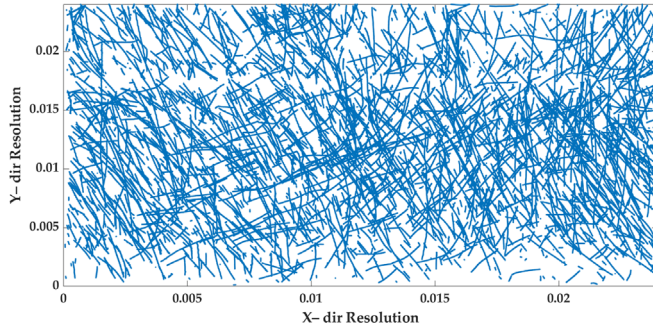
FIG. 6. Real view of the path traveled by the particles, obtained from the video recordings for a data set that included 4000 images (resolution of 512 × 512 pixels), obtained from one of the 20 individual and independent videos observing the same experimental condition.

involved tracks are stopped at the frame $[n]$, and a new track is considered to have begun in the frame $[n+1]$. Note that our LPT code for identifying and tracking the tracer particles is based on the work of Ouelette et al.[36]

V. RESULTS AND DISCUSSION
A. Turbulent flow quantities

Figure 6 presents real tracks from a run in an LPT experiment performed in the described facility. Turbulent flow quantities in the experiments are initially extracted to base the subsequent comparison on; this includes the energy dissipation rate, Kolmogorov length and timescale, and the turbulent Reynolds–Taylor microscale. PIV is applied for this purpose to the turbulent flow prior to the application of strain in a nearly stationary homogenous turbulent box flow. Figure 7 shows the compensated longitudinal structure function $D_{LL}(r)$ in terms of the separation r to evaluate the dissipation ϵ. Two cases are displayed based on the two turbulence intensities produced by the two motor speeds of the impellers driving the turbulent flow. In the inertial subrange, the compensated structure functions are nearly constant, allowing us to determine the dissipation rate ϵ in the flow (we use r between 60η and $l/6$ according to Ref. 1).

Table I summarizes the different cases under investigation, which are controlled by the rotation speed of the impellers in the
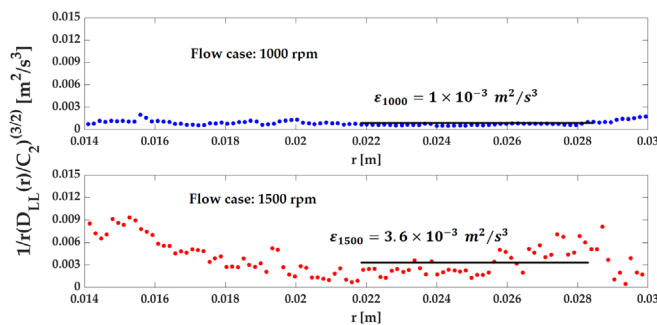

FIG. 7. Compensated second-order longitudinal structure functions $D_{LL}(r)$ via Eq. (4) for the flow cases $Re_{\lambda 1} = 110$; 1000 rpm and $Re_{\lambda 2} = 152$; 1500 rpm. The black lines indicate the expected value of the dissipation rate in each case. ϵ is the energy dissipation rate, $C_2 = 2.1$ is the universal constant,[1] and r is the separation.

TABLE I. Flow parameters obtained from PIV measurements for passive particles. ϵ, turbulence energy dissipation rate; ν, kinematic viscosity; l, large eddy length scale (integral scale); u_{rms}, velocity root mean square; η, Kolmogorov length scale; τ_η, Kolmogorov timescale; λ, Taylor microscale; Re_l, Reynolds number based on the length scale of the large eddies present in the flow; Re_λ, Reynolds–Taylor microscale.

Flow quantities	Flow case 1000 rpm	Flow case 1500 rpm
$\epsilon\,(\mathrm{m^2/s^3})$	1.0×10^{-3}	3.6×10^{-3}
$\nu\,(\mathrm{m^2/s})$	1×10^{-6}	1×10^{-6}
$l\,(\mathrm{cm})$	5.70	7.40
$u_{rms}\,(\mathrm{m/s})$	0.026	0.047
$\eta = (\nu^3/\epsilon)^{1/4}\,(\mathrm{mm})$	0.177	0.129
$\tau_\eta = (\nu/\epsilon)^{1/2}\,(\mathrm{ms})$	31.6	16.6
$\lambda = (15\nu/\epsilon)^{1/2}\,(\mathrm{mm})$	3.8	3.2
$Re_l = u_{rms}l/\nu$	1485	3478
$Re_\lambda = u_{rms}\lambda/\nu$	110	152

experimental facility. Once the dissipation and velocity RMS are measured, the remaining quantities are known.

B. Particle characterization

Table II summarizes the properties of the particles seeded in the flow. The Stokes numbers are calculated based on Eq. (9), e.g., the ratio of the particle response and the timescale of the flow presented. It must be noted that the particle Stokes numbers are based on the Kolmogorov timescale of the flow before the straining motion is applied to the turbulent field. Although it is expected that the timescale in the flow changes during the deforming motion, observations are assumed on the Stokes number's initial value. In addition, it is expected that the short duration of the straining motion will not affect the smallest scales of motion in the turbulent flow field to a high degree. The Stokes number for tracer and inertial particles are in the range of 0.006 32–0.018 07 and 0.113–0.307, respectively.

C. Mean strain motion

In this study, the experiment is conducted with a novel approach to simulate a strain flow with a specified mean strain rate. Figure 8 indicates the mean strain measurement for $2S = 4\,\mathrm{s}^{-1}$ for both flow cases. The results show that the turbulence flow reaches the mean

TABLE II. Stokes number for the two types of particles applied in the experiments. Buoyant and Inertial particles with several flow cases.

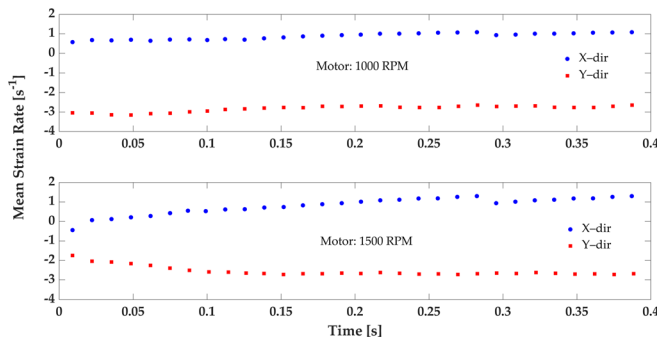| Particle Type	Size $d_p(\mu m)$	Flow case $Re_{\lambda 1} = 110$; 1000 rpm $\tau_\eta = 31.6$ ms Stokes number	Flow case $Re_{\lambda 2} = 152$; 1500 rpm $\tau_\eta = 16.6\,ms$ Stokes number
Tracer	(Min.) 8	6.32×10^{-3}	12.04×10^{-3}
	(Max.) 10	9.49×10^{-3}	18.07×10^{-3}
Inertial	(Min.) 210	0.113	0.216
	(Max.) 250	0.161	0.307

FIG. 8. A presentation of the mean strain rate is measured for the flow during the straining generation for tracer particles. The strain is conducted in Y-dir with $-4\,\text{s}^{-1}$ and in X-dir $2\,\text{s}^{-1}$. The filled blue circle is for the X-dir, and the filled red square is for Y-dir. The above drawing is for flow case $Re_{\lambda 1} = 110$; 1000 rpm, and down curves are for flow case $Re_{\lambda 2} = 152$; 1500 rpm.

strain rate during strain generation in the main direction y as $-4\,\text{s}^{-1}$ and the x direction is $2\,\text{s}^{-1}$ based on Eq. (1) for mean strain. Figure 9, in the same manner, dictates the mean strain measurement for $2S = 8\,\text{s}^{-1}$ for both flow cases. The mean strain rate for $2S = 4\,\text{s}^{-1}$ was achieved approximately with a 15% difference from the theoretical strain rate, but for $2S = 8\,\text{s}^{-1}$, the measured mean strain rate reached the theoretical rate accurately. The reason for this distinction is not apparent, but it seems that for a lower strain rate, the tracer particles need more time to attain the theoretical rate because of the large-scale eddies effects and rate of energy transfer. The literature notes that the external motion and energy source moving on the flow, such as strain or shear, could drive instability in the flow.[1,17,20] It could be another reason to see a less achieved strain rate for the case flow with $2S = 4\,\text{s}^{-1}$. Results for the strain measurement have been earned based on the tracer particles. These measurements show that the experiment simulated the strain motion with the desired outcomes, matching the strain motion behavior quantitatively and qualitatively.

D. Velocity root mean square (RMS)

Figures 10 and 11 show that for the tracer particles with equal turbulence intensity, the velocity RMS component in the y-direction is
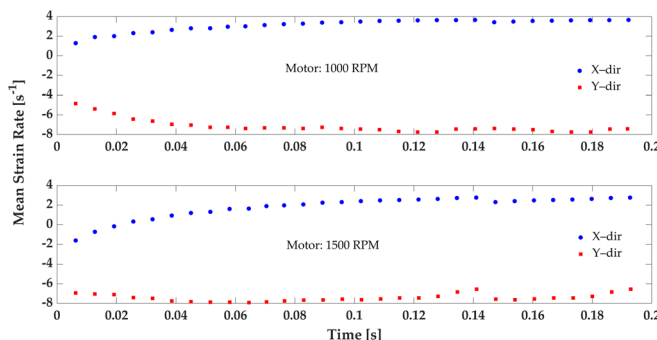

FIG. 9. A presentation of the mean strain rate is measured for the flow during the straining generation for tracer particles. The strain is conducted in Y-dir with $-8\,\text{s}^{-1}$ and in X-dir $4\,\text{s}^{-1}$. The filled blue circle is for the X-dir, and the filled red square is for Y-dir. The above drawing is for flow case $Re_{\lambda 1} = 110$; 1000 rpm, and the down curves are for flow case $Re_{\lambda 2} = 152$; 1500 rpm.
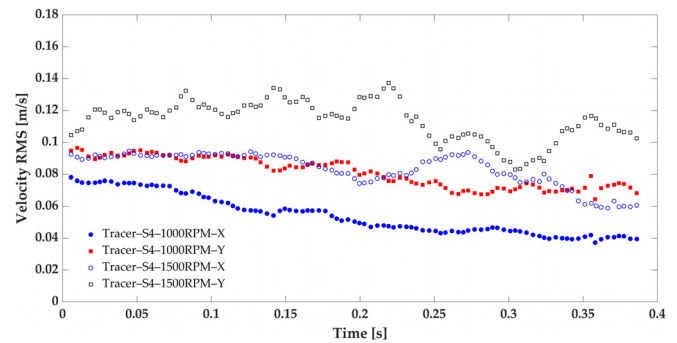

FIG. 10. The velocity RMS for the straining turbulence flow with $2S = 4\,\text{s}^{-1}$ and flow cases $Re_{\lambda 1} = 110$; 1000 rpm and $Re_{\lambda 2} = 152$; 1500 rpm for X and Y components for tracer particles. The filled blue circle, the empty blue circle, the filled red square, and the empty black square represent X-dir; flow case $Re_{\lambda 1}$, X-dir, flow case $Re_{\lambda 2}$, Y-dir; flow case $Re_{\lambda 1}$ and Y-dir, flow case $Re_{\lambda 2}$, respectively.

more extensive than in the x-direction, as the strain motion in the y-direction has a double mean strain rate than the other direction. However, for tracers with a similar mean strain rate, the flow case with intense turbulence has higher velocity RMS and amplitude fluctuation.

In the literature, it has been noticed that the strain motion could generate extra oscillation and increase the fluctuation.[20,21] Figures 10 and 11 illustrate that tracer particles with the same direction and equal turbulence intensity have gained intensive fluctuation with a higher mean strain rate. Moreover, since all flow cases approximately had the same initial condition before the strain, the results showed the velocity RMS is not only related to the initial condition but also affected by the history of the turbulence.[20]

Figures 12 and 13 display that strain motion has affected the inertial particle, and velocity RMS has fluctuated much more. The inertial particle has more substantial oscillations than tracers for cases with analogous mean strain rate and turbulence intensity. Figures 12 and 13 represent that the inertial particles in the flow with higher turbulence intensity are much more sensitive to the strain motion and have profound effects than lower turbulence flow. This issue could be caused by scale distinction for flow with different turbulence intensities. In the previous studies, it has been noted that the large scale could
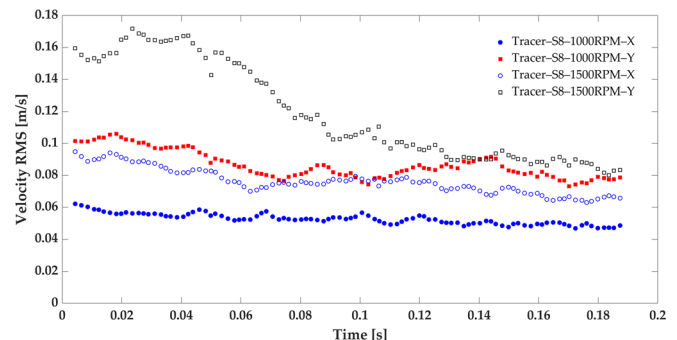

FIG. 11. The velocity RMS for the straining turbulence flow with $2S = 8\,\text{s}^{-1}$ and flow cases $Re_{\lambda 1} = 110$; 1000 rpm and $Re_{\lambda 2} = 152$; 1500 rpm for X and Y components for tracer particles. The filled blue circle, the empty blue circle, the filled red square, and the empty black square represent for X-dir; flow case $Re_{\lambda 1}$, X-dir, flow case $Re_{\lambda 2}$, Y-dir; flow case $Re_{\lambda 1}$ and Y-dir, flow case $Re_{\lambda 2}$, respectively.
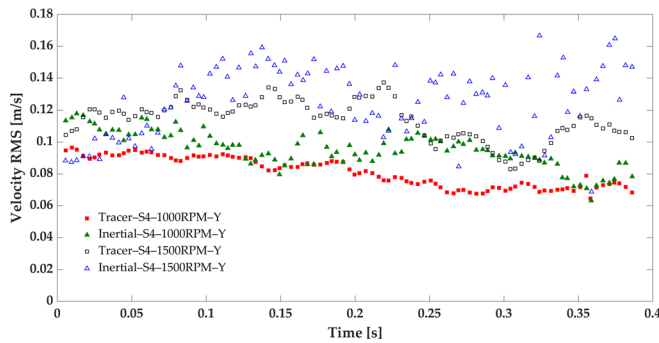
FIG. 12. The velocity RMS for the straining turbulence flow with $2S = 4\,\mathrm{s}^{-1}$ and flow cases $Re_{\lambda 1} = 110$; 1000 rpm and $Re_{\lambda 2} = 152$; 1500 rpm for Y component for tracer and inertial particles. The filled red square, the empty black square, the filled green triangle, and the empty blue triangle represent tracer; Y-dir; flow case $Re_{\lambda 1}$, tracer; Y-dir, flow case $Re_{\lambda 2}$, inertial; Y-dir; flow case $Re_{\lambda 1}$ and inertial; Y-dir, flow case $Re_{\lambda 2}$, respectively.
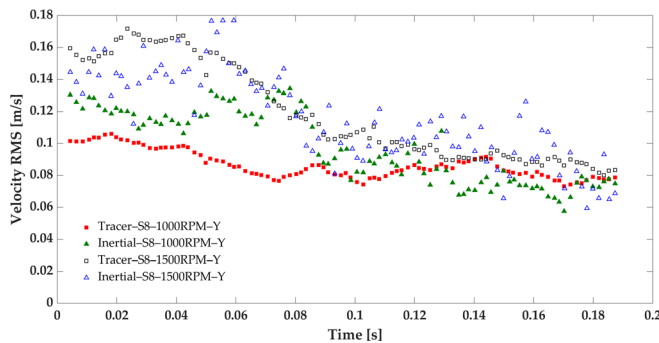

FIG. 14. The normalized Reynolds stress for the straining turbulence flow with $2S = 4\,\mathrm{s}^{-1}$ and flow case $Re_{\lambda 1} = 110$; 1000 rpm for Y component for tracer and inertial particles. The red-filled square, the filled blue circle, the filled green triangle, and the empty black diamond represent the normalized Reynolds stress in the Y direction for the tracer, in the X direction for the tracer, the Y direction for the inertial particle, and in the X direction for the inertial particle, respectively.

FIG. 13. The velocity RMS for the straining turbulence flow with $2S = 8\,\mathrm{s}^{-1}$ and flow cases $Re_{\lambda 1} = 110$; 1000 rpm and $Re_{\lambda 2} = 152$; 1500 rpm for Y component for tracer and inertial particles. The filled red square, the empty black square, the filled green triangle, and the empty blue triangle represent tracer; Y-dir; flow case $Re_{\lambda 1}$, tracer; Y-dir, flow case $Re_{\lambda 2}$, inertial; Y-dir; flow case $Re_{\lambda 1}$ and inertial; Y-dir, flow case $Re_{\lambda 2}$, respectively.

FIG. 15. The normalized Reynolds stress for the straining turbulence flow with $2S = 8\,\mathrm{s}^{-1}$ and flow case $Re_{\lambda 1} = 110$; 1000 rpm for Y component for tracer and inertial particles. The red-filled square, the filled blue circle, the filled green triangle, and the empty black diamond represent the normalized Reynolds stress in the Y direction for the tracer, in the X direction for the tracer, the Y direction for the inertial particle, and in the X direction for the inertial particle, respectively.

noticeably affect particle motion.[17,20] However, because the inertial particle is denser than the tracer, the gravity effect could be considered the second effective parameter in addition to strain motion.

E. Normalized Reynolds-stress in the strained turbulent flow

As described in the theory section, the Reynolds-stress is an appropriate term to assess the fluctuation effects. Figures 14–17 show the normalized Reynolds-stress and determine that the denser particle gains an intensive effect from the strain motion than the tracer in the same condition. Moreover, the inertial particles with similar straining turbulence flow have less sensitivity to the strain motion in flow with higher turbulence intensity. It results in the same manner for tracer and inertial particles and must be taken as a specific issue regarding the scale size for distinct turbulence flow. However, we must notice that the gravity effect for the inertial particle could increase the strain motion impact. In this practical study, gravity is a parameter not
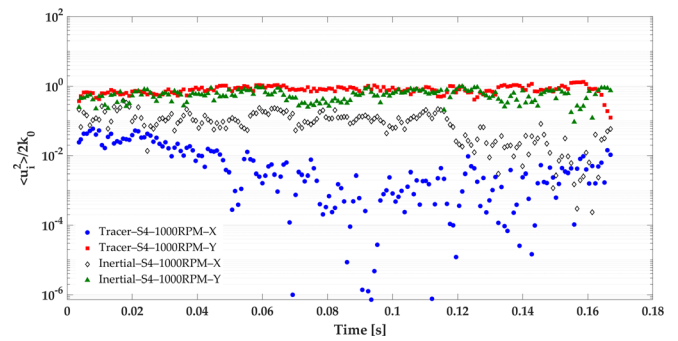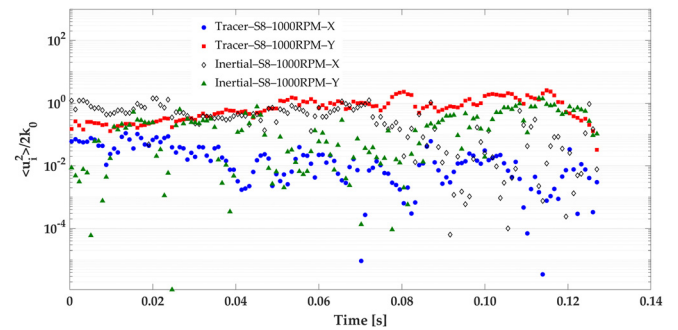

FIG. 16. The normalized Reynolds stress for the straining turbulence flow with $2S = 4\,\mathrm{s}^{-1}$ and flow case $Re_{\lambda 2} = 152$; 1500 rpm for Y component for tracer and inertial particles. The red-filled square, the filled blue circle, the filled green triangle, and the empty black diamond represent the normalized Reynolds stress in the X direction for the tracer, in the Y direction for the tracer, the Y direction for the inertial particle, and in the X direction for the inertial particle, respectively.
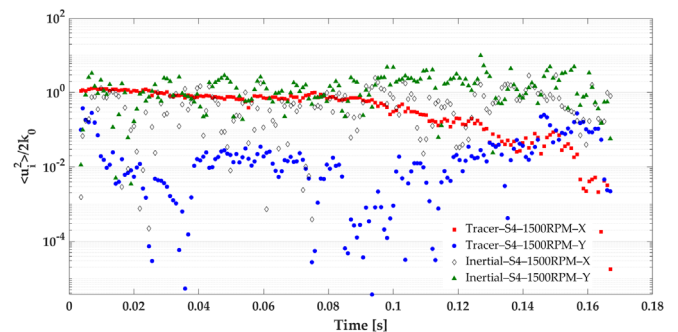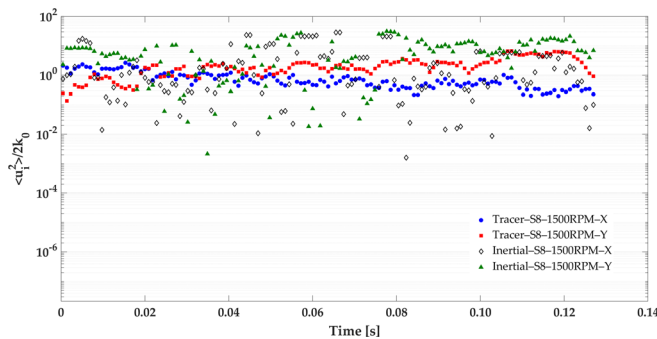
20 January 2025 14:54:21

FIG. 17. The normalized Reynolds stress for the straining turbulence flow with $2S = 8\,\mathrm{s}^{-1}$ and flow case $Re_{\lambda 2} = 152$; 1500 rpm for Y component for tracer and inertial particles. The red-filled square, the filled blue circle, the filled green triangle, and the empty black diamond represent the normalized Reynolds stress in the Y direction for the tracer, in the X direction for the tracer, the Y direction for the inertial particle, and in the X direction for the inertial particle, respectively.

considered in previous numerical works, and the observation in this study appears that gravity affects inertial particles' behavior more than tracer particles.

VI. CONCLUSIONS

First, this study aims to design a novel experimental procedure to generate a straining deformation in turbulence flow, and second, to investigate the Lagrangian dynamics of tracer and inertial particles affected by flow distortion practically in the presence of gravity. The Lagrangian particle tracking method and particle image velocimetry approach were employed to extract particle statistics and flow characterizations from the videos recorded by a high-speed camera, respectively. In the first step, the outcome of strain motion measurements showed that the designed experiment matched the desired state with remarkable results. The measured strain rate intensively corresponds to the theoretical mean strain rate and can be used to create a straining turbulence flow with a different mean strain rate in this approach. The considerable observation is related to the sensitivity of the conducted strain rate. The results depict that the high mean strain rate made its effect faster than the lower mean strain rate on the flow with similar turbulence intensity. This behavior could be related to large-scale interactions and how energy transfers to small scales. In the next step, post-processing on the particle statistics presents us with velocity RMS and Reynolds-stress. The results illustrate that the geometry of the flow or distortion affects the inertial particles more extensively than the tracer particles. The inertial particles in the flow with extreme turbulence intensity have less sensitivity to distortion. It seems the presence of gravity causes distortion effects to be increased on the dynamics of the inertial particles. The results of this study can be listed as follows:

- The strain motion has been affected by both tracer and inertial particles.
- Inertial particles have a more intensive impact from the strain motion than tracer particles.
- For two flow cases with distinct turbulence intensities, there are observations regarding scale size, leading to some effects on particle motion.

- The results illustrate that the strain motion eventually generates extra fluctuation, increasing the fluctuation amplitude increased than without strain.
- The Reynolds-stress results represent that they are affected by the initial condition, strain motion, and history of the turbulence.
- Although the inertial particle is heavier than the tracer, it could be effective by gravity added to the strain motion impact for these types of particles.

AUTHOR DECLARATIONS
Conflict of Interest

The authors have no conflicts to disclose.

Author Contributions

Reza Hassanian: Conceptualization (equal); Investigation (equal); Methodology (equal); Software (equal); Validation (equal); Visualization (equal); Writing – original draft (equal). **Ásdís Helgadóttir:** Supervision (equal); Writing – review & editing (equal). **Lahcen Bouhlali:** Formal analysis (equal); Methodology (equal); Software (equal). **Morris Riedel:** Funding acquisition (equal); Supervision (equal); Writing – review & editing (equal).

DATA AVAILABILITY

The data that support the findings of this study are available from the corresponding author upon reasonable request.

REFERENCES

[1]S. B. Pope, *Turbulent Flows* (Cambridge University Press, 2000).
[2]R. A. Shaw, "Particle-turbulence interactions in atmospheric clouds," Annu. Rev. Fluid Mech. **35**, 183–227 (2003).
[3]F. Toschi and E. Bodenschatz, "Lagrangian properties of particles in turbulence," Annu. Rev. Fluid Mech. **41**, 375–404 (2009).
[4]G. Yeoh, J. J. Chen, and C. H. Chen, "Investigation of swirling flows in mixing chambers," Modell. Simul. Eng. **2011**, 259401.
[5]M. H. Arabnejad, A. Amini, M. Farhat, and R. E. Bensow, "Numerical and experimental investigation of shedding mechanisms from leading-edge cavitation," Int. J. Multiphase Flow **119**, 123–143 (2019).
[6]T. Tanuma, *Advances in Steam Turbines for Modern Power Plants* (Woodhead Publishing, 2017).
[7]B. Taherkhani, A. P. Anaraki, J. Kadkhodapour, N. K. Farahani, and H. Tu, "Erosion due to solid particle impact on the turbine blade: Experiment and simulation," J. Failure Anal. Prev. **19**, 1739–1744 (2019).
[8]G. K. Batchelor, *The Theory of Homogeneous Turbulence* (Cambridge University Press, 1982).

[9] J. C. R. Hunt, "A theory of turbulent flow round two-dimensional bluff bodies," J. Fluid Mech. **61**, 625–706 (1973).

[10] Z. Warhaft, "An experimental study of the effect of uniform strain on thermal fluctuations in grid-generated turbulence," J. Fluid Mech. **99**, 545–573 (1980).

[11] J. C. R. Hunt and D. J. Carruthers, "Rapid distortion theory and the 'problems' of turbulence," J. Fluid Mech. **212**, 497–532 (1990).

[12] S. Ayyalasomayajula and Z. Warhaft, "Nonlinear interactions in strained axisymmetric high-Reynolds-number turbulence," J. Fluid Mech. **566**, 273–307 (2006).

[13] J. Chen, C. Meneveau, and J. Katz, "Scale interactions of turbulence subjected to a straining-relaxation-destraining cycle," J. Fluid Mech. **562**, 123–150 (2006).

[14] P. Gualtieri and C. Meneveau, "Direct numerical simulations of turbulence subjected to a straining and destraining cycle," Phys. Fluids **22**, 065104 (2010).

[15] L. J. Baker and F. Coletti, "Particle-fluid-wall interaction of inertial spherical particles in a turbulent boundary layer," J. Fluid Mech. **908**, A39 (2021).

[16] W. Xiao, T. Jin, K. Luo, Q. Dai, and J. Fan, "Eulerian-Lagrangian direct numerical simulation of preferential accumulation of inertial particles in a compressible turbulent boundary layer," J. Fluid Mech. **903**, A19 (2020).

[17] C.-M. Lee, Á. Gylfason, P. Perlekar, and F. Toschi, "Inertial particle acceleration in strained turbulence," J. Fluid Mech. **785**, 31–53 (2015).

[18] A. Klein, "Characteristics of combustor diffusers," Prog. Aerosp. Sci. **31**, 171–271 (1995).

[19] Z. Han and R. D. Reitz, "Turbulence modeling of internal combustion engines using RNG κ-ε models," Combust. Sci. Technol. **106**, 267–295 (1995).

[20] P. A. Davidson, *Turbulence: An Introduction for Scientists and Engineers* (Oxford University Press, 2004).

[21] H. T. John and L. Lumley, *A First Course in Turbulence* (MIT Press, 1972).

[22] R. Hassanian, s Helgadóttir, and M. Riedel, "Deep learning forecasts a strained turbulent flow velocity field in temporal Lagrangian framework: Comparison of LSTM and GRU," Fluids **7**, 344 (2022).

[23] P. J. Ireland, A. D. Bragg, and L. R. Collins, "The effect of Reynolds number on inertial particle dynamics in isotropic turbulence. Part 1. Simulations without gravitational effects," J. Fluid Mech. **796**, 617–658 (2016).

[24] L. Biferale and I. Procaccia, "Anisotropy in turbulent flows and in turbulent transport," Phys. Rep. **414**, 43–164 (2005).

[25] A. J. Petersen, L. Baker, and F. Coletti, "Experimental study of inertial particles clustering and settling in homogeneous turbulence," J. Fluid Mech. **864**, 925–970 (2019).

[26] J. Lee and C. Lee, "The effect of wall-normal gravity on particle-laden near-wall turbulence," J. Fluid Mech. **873**, 475–507 (2019).

[27] L. Brandt and F. Coletti, "Particle-laden turbulence: Progress and perspectives," Annu. Rev. Fluid Mech. **54**, 159–189 (2022).

[28] M. Mehrabadi, J. A. K. Horwitz, S. Subramaniam, and A. Mani, "A direct comparison of particle-resolved and point-particle methods in decaying turbulence," J. Fluid Mech. **850**, 336–369 (2018).

[29] M. Momenifar and A. D. Bragg, "Local analysis of the clustering, velocities, and accelerations of particles settling in turbulence," Phys. Rev. Fluids **5**, 034306 (2020).

[30] H. Xia, N. Francois, H. Punzmann, and M. Shats, "Lagrangian scale of particle dispersion in turbulence," Nat. Commun. **4**, 2013 (2013).

[31] R. Hassanian, "An experimental study of inertial particles in deforming turbulence flow, in context to loitering of blades in wind turbines," M.S. dissertation (Reykjavik University, 2020).

[32] L. Bouhlali, "On the effects of buoyancy on passive particle motions in the convective boundary layer from the Lagrangian viewpoint," M.S. dissertation (Reykjavik University, 2012).

[33] M. R. J. Kompenhans, C. E. Willert, F. Scarano, C. J. Kähler, and S. T. Wereley, *Particle Image Velocimetry* (Springer International Publishing, 2018).

[34] R. J. Adrian and R. D. Keane, "Theory of cross-correlation analysis of PIV images," Appl. Sci. Res. **49**, 191 (1992).

[35] E. A. Cowen, S. G. Monismith, E. A. Cowen, and S. G. Monismith, "A hybrid digital particle tracking velocimetry technique," Exp. Fluids **22**, 199–211 (1997).

[36] N. T. Ouellette, H. Xu, and E. Bodenschatz, "A quantitative study of three-dimensional Lagrangian particle tracking algorithms," Exp. Fluids **40**, 301–313 (2006).

20 January 2025 14:54:21